

# Investigating a Seemingly Simple Imine-Linked Covalent Organic Framework Structure

Cailing Chen,<sup>††</sup> Li Cao,<sup>††</sup> Yaozu Liu,<sup>††</sup> Zhihao Li,<sup>††</sup> Zhen-Hua Li,<sup>††</sup> Guojun Zhou, Daliang Zhang,\*  
Xuehai Huang, Yu Wang,\* Guanxing Li, Lingmei Liu, You-You Yuan, Yaping Zhang, Qingxiao Wang,  
Yiqiang Chen, Zhan Shi, Qianrong Fang, Zhehao Huang,\* Zhiping Lai,\* and Yu Han\*



Cite This: <https://doi.org/10.1021/jacs.4c16678>



Read Online

ACCESS |



Metrics & More

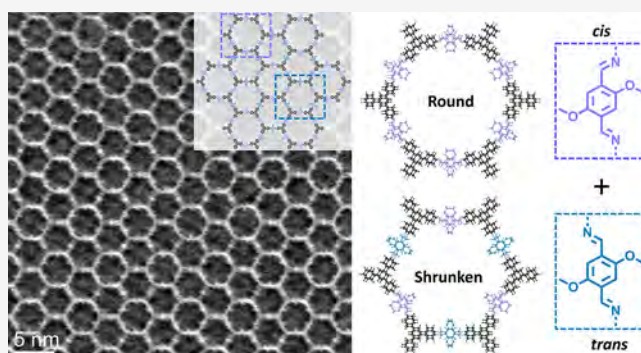


Article Recommendations



Supporting Information

**ABSTRACT:** The structures of covalent organic frameworks (COFs) are typically determined through modeling based on powder X-ray diffraction. However, the intrinsically limited crystallinity of COFs often results in structural determinations of low fidelity. Here, we present real-space imaging of an extensively studied two-dimensional imine-based COF. Contrary to the conventional understanding that this COF features uniform hexagonal pores, our observations reveal the presence of two distinct sets of pores with differences in shape and size. Motivated by this finding, we conducted reciprocal-space characterizations, complemented by solid-state nuclear magnetic resonance spectroscopy and density functional theory calculations, to reevaluate this seemingly simple structure. The collective results allow for the establishment of a new structural model for this landmark COF and its derivatives, differing from the conventional model in both intra- and interlayer configurations. Furthermore, we identified various previously unrecognized defective structures through real-space imaging, which have significant implications for COF applications in separation and catalysis. Our study demonstrates the complexity and heterogeneity of COF structures, while also highlighting the imperative for structural reevaluation using advanced characterization techniques.



## INTRODUCTION

Determining the structures of materials is essential for understanding their properties, yet it is a nontrivial task. Advances in characterization techniques can transform traditional views by providing greater precision in structural determination. For instance, single-layer graphite, known as graphene, was once thought to be unstable in nature, but its existence was later demonstrated through the combination of various imaging and spectroscopy techniques.<sup>1</sup> Similarly, liquid water was long considered to consist of randomly distributed molecules. However, neutron and X-ray scattering, as well as X-ray absorption spectroscopy, have revealed the presence of local structural order within its highly dynamic hydrogen bond network, although the specific local symmetry remains controversial.<sup>2–5</sup>

Covalent organic frameworks (COFs) constitute a novel class of porous crystalline materials,<sup>6–9</sup> with significant applications in catalysis, adsorption, separation, and sensing.<sup>10–13</sup> Due to the difficulty in growing large single crystals of COFs, their bulk structures are typically determined through modeling based on structural building units and chemical linkages, refined using powder X-ray diffraction data.<sup>14–17</sup> This method, however, has inherent limitations in accuracy. Additionally, probing local

structural features such as grain boundaries and point defects in COFs is challenging,<sup>18–21</sup> because transmission electron microscopy (TEM), the most suitable tool for this purpose, is constrained by the high sensitivity of COFs to electron beam irradiation.

COFs constructed using imine linkages via Schiff base chemistry have been extensively investigated due to the high reversibility of bond formation and the wide range of available monomers.<sup>22–27</sup> Among these imine-linked COFs, a material synthesized from 1,3,5-tris(4-aminophenyl)benzene (TAPB) and 2,5-dimethoxyterephthalaldehyde (DMPDA), denoted as TAPB-DMPDA, has garnered widespread attention due to its exceptional crystallinity and substantial porosity.<sup>10,14,17,28–32</sup> Considering the connectivity of its monomers, TAPB-DMPDA is believed to possess a straightforward two-dimensional (2D) structure: an ordered porous framework extending in two

**Received:** November 23, 2024

**Revised:** December 5, 2024

**Accepted:** December 6, 2024

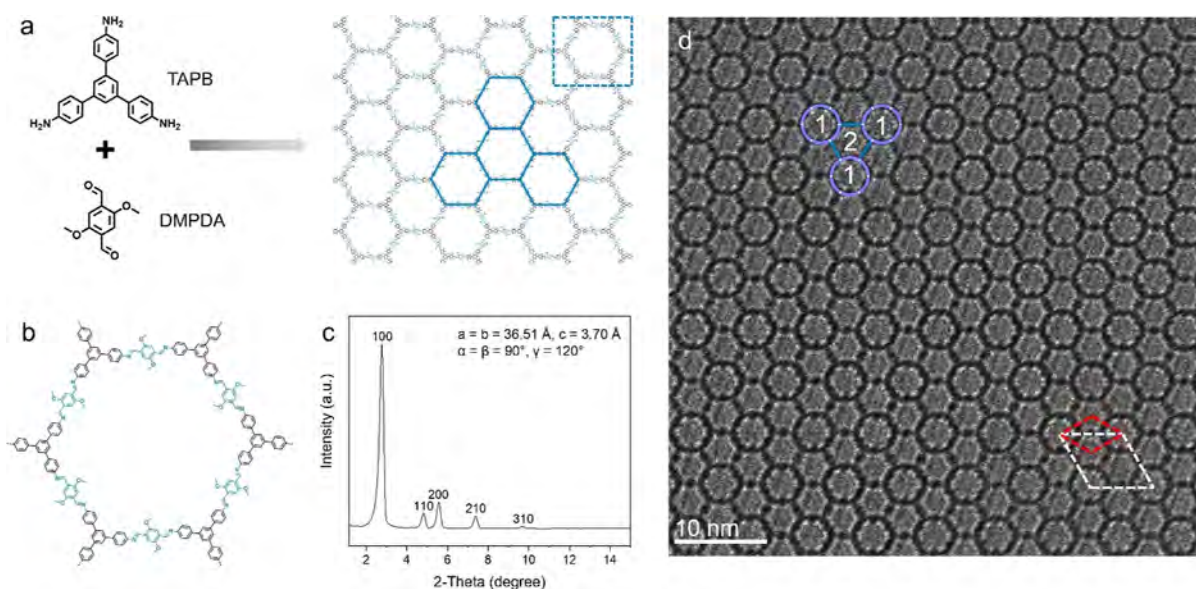


**Figure 1.** Comparison of generally accepted and HRTEM-observed structures of TAPB-DMPDA. (a) Schematic illustration of the synthesis of TAPB-DMPDA via a Schiff-base condensation reaction, with its structure depicted according to the generally accepted model, where turquoise hexagons delineate identical 6-MR pores. (b) Enlarged view of a single 6-MR pore marked in a, showing that the diimine linkages exclusively adopt the *trans* conformation. (c) PXRD pattern of TAPB-DMPDA, indexed based on the generally accepted monopore structure model. (d) ULD-HRTEM image of TAPB-DMPDA acquired along the [001] direction, showing two types of 6-MR pores with different shapes, labeled 1 and 2, respectively. The unit cells of the monopore and dual-pore structures are delineated with red and white rhombuses, respectively.

dimensions with layers stacking in the third dimension, where each layer contains identical six-membered ring (6-MR) pores in a regular hexagonal shape, and all layers are aligned, resulting in 6-MR straight channels running throughout the stacked layers.

Here, we reexamined this widely studied COF using advanced characterization techniques, including ultralow-dose high-resolution TEM (ULD-HRTEM), small-angle X-ray scattering (SAXS), three-dimensional electron diffraction (3DED), and two-dimensional nuclear magnetic resonance (2D-NMR) spectroscopy. Our results explicitly demonstrate that, contrary to the generally accepted view that TAPB-DMPDA has identical 6-MR channels, it actually possesses two sets of 6-MR channels that differ in shape and diameter. This finding suggests the coexistence of *cis* and *trans* diimine linkages within this COF. Our results also reveal that adjacent layers are flipped relative to each other, contradicting the conventional structural model in which all layers share the same configuration. Theoretical calculations indicated that the newly identified dual-pore AA'-stacking structure is thermodynamically more favorable than the previously assumed monopore AA-stacking structure, as it leads to significantly stronger interlayer interactions. Furthermore, TAPB-DMPDA samples synthesized under varying conditions, as well as two derivatives incorporating different side groups, consistently exhibit the dual-pore structure, confirming its universality. In addition, using ULD-HRTEM, we directly observed abundant grain boundaries composed of 5-, 7-, and 8-MR pores, and established their correlation with grain orientations. Given that the most crucial characteristic of crystalline porous materials is their size- and shape-selectivity, the discovery of the previously unknown dual-pore structure and diverse local non-6-MR structures has significant implications for the applications of TAPB-DMPDA and related COFs in catalysis and separation.

## RESULTS AND DISCUSSION

**Structural Determination of TAPB-DMPDA.** The construction of TAPB-DMPDA from two monomers through an aldehyde-amine condensation reaction is schematically illustrated in Figure 1a. This COF was first reported by Jiang's group<sup>10</sup> and later widely reproduced by other groups using the same or modified synthetic methods.<sup>29,33,34</sup> The resultant materials are consistently described as having a 2D hexagonal layered structure. Each layer consists of identical 6-MR pores in regular hexagonal shapes (Figure 1a), with all layers being identical and aligned in an AA-stacking mode.<sup>10,14,29,30</sup> The diimine linkages connecting two nodes are generally considered to adopt the *trans* conformation (see Figure 1b) to maintain the regular hexagonal pore structure extending throughout the layer.

We chose to use the method developed by Dichtel's group to synthesize TAPB-DMPDA, as it yields products with exceptionally high crystallinity.<sup>29</sup> We performed the synthetic reaction at 150 °C for 1 h before collecting the product. The detailed synthesis procedure is provided in the Materials and Methods section. The obtained COF consists of plate-like crystals with diameters of 1–2 μm (Figure S1). Atomic force microscopy reveals that these platelets are as thin as ~20 nm at their peripheries (Figure S2), making them ideal for HRTEM imaging. Powder X-ray diffraction (PXRD) using Cu Kα radiation exhibits five clearly discernible peaks in the 2θ range of 2–10° (Figure 1c), which are assigned in the literature to the 100, 110, 200, 210, and 310 reflections of a hexagonal lattice. Following this assignment, the unit cell parameter of the synthesized TAPB-DMPDA sample is  $a = b = 36.51 \text{ \AA}$ , in good agreement with the previously reported results for this COF. In the literature, the unit cell parameter  $c$  is determined from the peak at  $2\theta \approx 26^\circ$  to be approximately 3.7 Å, assuming the AA stacking mode.

We employed ULD-HRTEM real-space imaging<sup>35–39</sup> to examine the structure of TAPB-DMPDA. The images were

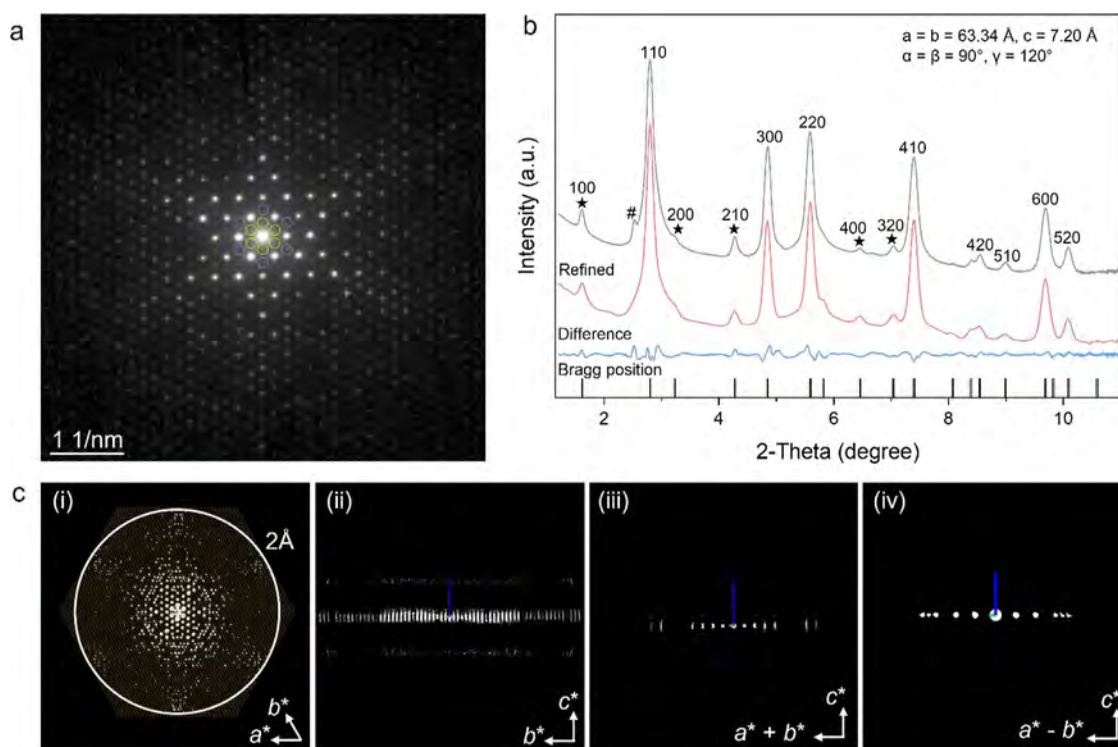


**Figure 2.** Electron diffraction and X-ray scattering characterizations of TAPB-DMPDA. (a) SAED pattern acquired along the  $[001]$  direction. The yellow circles and violet circles mark the  $\{100\}$  and  $\{200\}$  diffraction spots, respectively, which were overlooked in earlier studies. Note that  $\{100\}$  represents the six equivalent planes:  $(100)$ ,  $(010)$ ,  $(-110)$ ,  $(-100)$ ,  $(0-10)$ , and  $(1-10)$ . (b) Experimental and refined ( $R_{wp} = 3.53\%$ ,  $R_p = 2.77\%$ ) SAXS patterns, indexed based on the dual-pore structure. Asterisks indicate the peaks missed in previous PXRD studies. The hash mark indicates the only unindexed peak, which may arise from impurities (see Figure S6 for further discussion). (c) 3D reciprocal lattice reconstructed from 3DED data, viewed along the (i)  $[001]$  and (ii)  $[100]$  directions. 2D slice cuts show the (iii)  $h\bar{h}2\bar{h}l$  and (iv)  $h\bar{h}0l$  planes. Red, green, and blue lines represent the lengths of the three basis vectors of the reciprocal lattice ( $a^*$ ,  $b^*$ , and  $c^*$ ), respectively.

acquired along the channel direction with precisely controlled electron doses of less than  $10 \text{ e}^-/\text{\AA}^2$  to prevent structural damage, achieving a resolution greater than  $2.5 \text{ \AA}$  (Figure S3). Interestingly, the image reveals that, contrary to the generally accepted structural model featuring identical hexagonal pores (Figure 1a), this COF possesses two types of 6-MR pores that differ in shape (Figure 1d). One type consists of six convex edges, giving it a nearly round appearance, while the other combines three straight edges with three concave edges, resulting in shrunken pores with a smaller size (Figure 1d). To rule out the possibility that this unusual structure is an artifact of HRTEM, we employed another low-dose technique, integrated differential phase-contrast scanning TEM (iDPC-STEM), for cross-validation. The obtained images confirm the coexistence of round and shrunken pores in TAPB-DMPDA (Figure S4).

A reasonable explanation for the observed dual-pore structure is that *cis* and *trans* conformations of the diimine linkage coexist in the framework, corresponding to the curved and straight edges of the 6-MRs, respectively (Figure S5). However, a question arises: given that the unit cell of the dual-pore structure is apparently larger than that of the previously assumed monopore structure (Figure 1d), why has this larger unit cell not been identified in previous PXRD studies of this COF? We believe this can be attributed to the low sensitivity of PXRD to the reflections associated with the larger unit cell, which are generally weak due to the subtle difference between these two structures.

Inspired by the HRTEM observations, we reexamined the structure of TAPB-DMPDA by conducting selected-area

electron diffraction (SAED) and small-angle X-ray scattering (SAXS) characterizations, which are more sensitive to weak reflections. As expected, “extra” reflections with large  $d$ -spacings were observed in the SAED pattern (Figure 2a). Similarly, SAXS reveals a notable peak at  $2\theta \approx 1.6^\circ$ , along with several peaks at higher angles that were missed by PXRD, as indicated by asterisks in Figure 2b. These findings confirm the presence of a large unit cell at  $a = b = 63.34 \text{ \AA}$ .

Further, we conducted 3DED to comprehend the three-dimensional structure of TAPB-DMPDA. From the reconstructed 3D reciprocal lattice [Figure 2c(i,ii)], the unit cell parameters are determined to be  $a = 65.30 \text{ \AA}$ ,  $b = 63.84 \text{ \AA}$ ,  $c = 7.20 \text{ \AA}$ ,  $\alpha = 89.72^\circ$ ,  $\beta = 90.57^\circ$ , and  $\gamma = 118.94^\circ$ . The large unit cell can be more clearly recognized from the high-angle reflections at approximately  $4.0\text{--}2.0 \text{ \AA}$ . Further analysis of the reflection conditions reveals the Laue class of  $6/mmm$ , indicating a hexagonal crystal system. The 2D slice cuts of the 3D reciprocal lattice exhibit reflection conditions as  $h\bar{h}2\bar{h}l$ :  $l = 2n$ ;  $h\bar{h}0l$ :  $l = 2n$  [Figure 2c(iii,iv)]. Therefore, the possible space groups for TAPB-DMPDA are  $P6cc$  (no. 184) and  $P6/mcc$  (no. 192). Eight 3DED data sets (Table S1) were merged for structural analysis, achieving a completeness of 75.7%, and a resolution of  $1.97 \text{ \AA}$ . Although this resolution was not sufficient for *ab initio* structure solution, the rendered electrostatic potential map exhibits a dual-pore structure, with the shapes of the two types of pores being consistent with the ULD-HRTEM and iDPC-STEM observations (see Figure 3b). In addition to confirming the dual-pore structure, the most crucial information from 3DED is that the unit cell parameter  $c$  is twice as large as

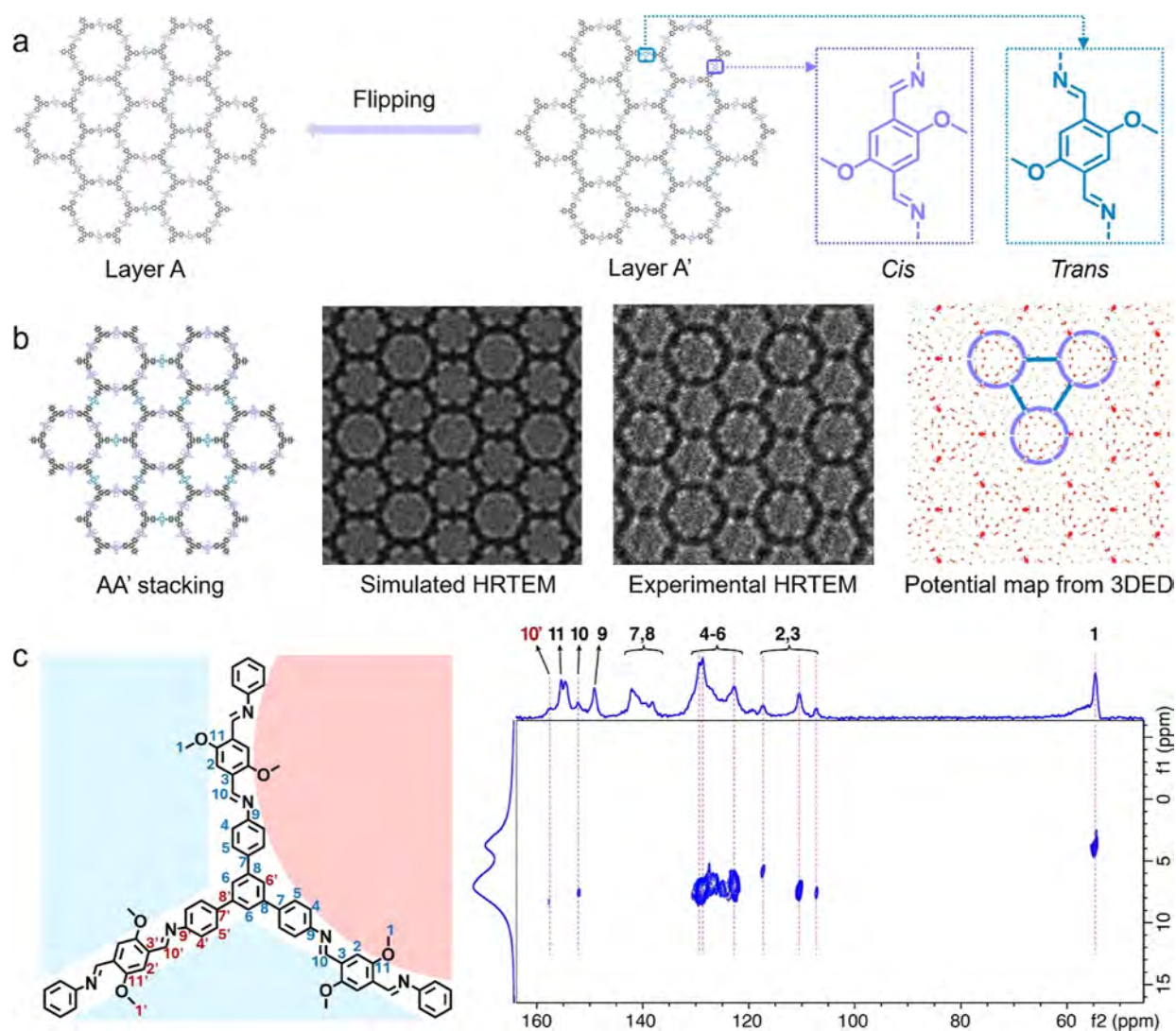


**Figure 3.** Validation of the dual-pore AA'-stacking structure of TAPB-DMPDA. (a) Schematic representation of the dual-pore AA'-stacking structure. Each layer features two types of 6-MR pores, resulting from the coexistence of *cis* and *trans* conformations of the diimine linkage in a 2:1 ratio. Adjacent layers (i.e., A and A') are oriented in a flipped arrangement relative to each other. (b) From left to right: projected structural model, simulated HRTEM image, experimental HRTEM image, and electrostatic potential map rendered from 3DED data. (c) Heteronuclear correlation  $^1\text{H}$ - $^{13}\text{C}$  NMR spectrum. The left panel shows the structural fragment of TAPB-DMPDA with two sets of chemically distinct carbon atoms labeled.

previously determined based on the AA stacking mode. The doubled unit cell size along the *c* direction can be explained by the COF adopting an AA' stacking mode, where adjacent layers are flipped relative to each other (Figure 3a).

Combining the results from ULD-HRTEM, SAXS and 3DED, we propose a new structural model for TAPB-DMPDA that differs from the widely accepted one in both the in-layer structure (dual-pore vs monopore) and the layer stacking mode (AA' stacking vs AA stacking). The newly identified structure, following geometry optimization using the Forcite module and refinement based on SAXS data via the Le Bail method (Table S2), was used for HRTEM simulation. The HRTEM image simulated with a specimen thickness of 20 nm and a defocus of  $-100$  nm exhibits a perfect match with the experimental image (Figure 3b). The effective diameters of the round and shrunken 6-MR pores, determined from the optimized structure, are approximately 32 and 30 Å, respectively (Figure S7). This difference is not distinguishable in the pore size distribution profile derived from the  $\text{N}_2$  sorption isotherm (Figure S8).

The dual-pore structure features coexisting *cis* and *trans* diimines in a 2:1 ratio, resulting in two sets of chemically distinct carbon atoms (11 types in each set) within the framework (Figure 3c). To differentiate the two sets of carbon atoms, we employed 600 MHz solid-state NMR and introduced heteronuclear correlation (HETCOR)  $^1\text{H}$ - $^{13}\text{C}$  spectroscopy. Due to the resolution limitations of solid-state NMR, most carbon atoms show broadened peaks, with their splitting not discernible in the HETCOR spectrum. However, the carbon atoms on the imine groups (i.e., carbon-10) exhibit two peaks with an area ratio of 2:1 (Figure 3c). This result provides additional evidence for TAPB-DMPDA having a dual-pore instead of a monopore structure.

It is noteworthy that while TAPB-DMPDA was traditionally believed to be composed solely of *trans* diimines, *cis* diimines have been identified in other COFs.<sup>24,25,27,40-42</sup> A recent study using single-crystal X-ray diffraction observed a *trans*-to-*cis* transition of diimines in COF Py-1P, accompanied by a change in stacking mode driven by loss of solvent.<sup>27</sup> The discovery of the coexistence of both *cis* and *trans* diimines in a COF in this

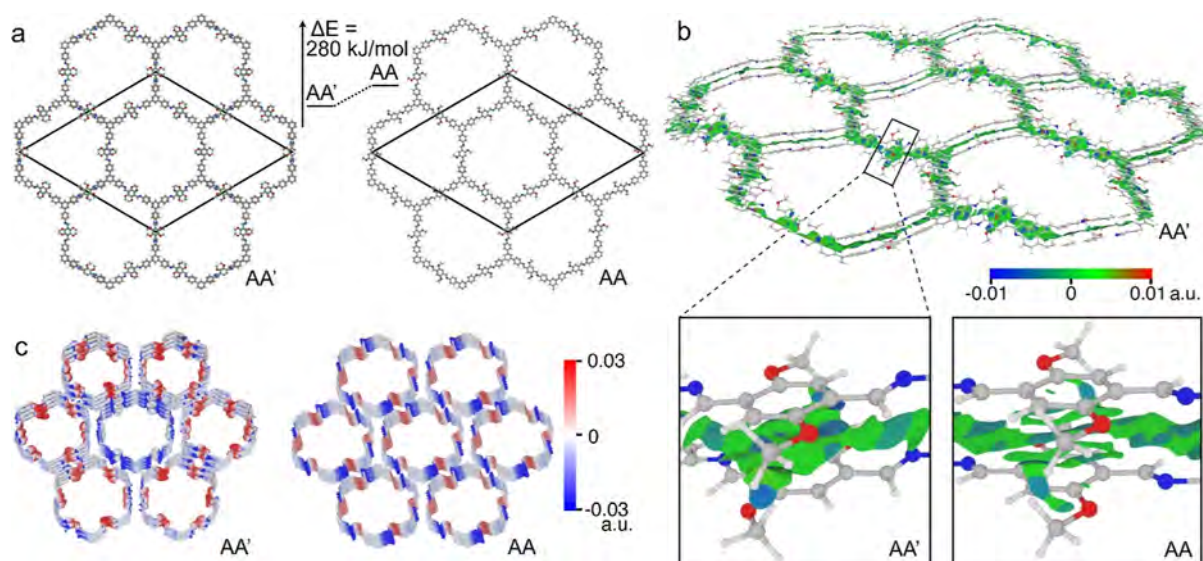


**Figure 4.** DFT calculations. (a) DFT-optimized structures for the dual-pore AA'-stacking and monopore AA-stacking models, along with their formation energy difference. (b) The noncovalent interaction isosurface of the dual-pore AA'-stacking structure, colored according to the  $\text{sign}(\lambda_2)\rho$  function. The local region between the dimethoxyphenyl moieties is enlarged for comparison with that of the monopore AA-stacking structure. (c) van der Waals surfaces projected with electrostatic potentials of the two structures, showing distinct charge distributions.

study adds a new dimension to our understanding, further highlighting the structural complexity of COFs.

**Theoretical Calculations.** Density functional theory (DFT) calculations reveal that the dual-pore AA'-stacking structure has a formation energy 280 kJ per mol unit cell (specific to the dual-pore structure) lower than that of the monopore AA-stacking structure (Figure 4a), indicating that it is the more thermodynamically favorable configuration. This substantial difference in formation energy is mainly attributed to the variation in noncovalent interlayer interactions, which is 223 kJ per mol unit cell, as determined by comparing the bulk and slab models. We further analyzed the noncovalent interaction (NCI) using Reduced Density Gradient function<sup>43</sup> and found that the interlayer interactions are primarily contributed by  $\pi$ - $\pi$  stacking, as shown by the NCI isosurfaces colored according to the  $\text{sign}(\lambda_2)\rho$  function. Notably, the NCI isosurface between the dimethoxyphenyl moieties is denser and energetically lower in the dual-pore AA'-stacking structure compared to the monopore AA-stacking structure, suggesting stronger local  $\pi$ - $\pi$  stacking (Figure 4b).

Figure 4c depicts the electrostatic potential on the van der Waals surfaces<sup>44</sup> of the two structures. The dual-pore AA' structure exhibits strong dipole separation, with the round channels being more negatively charged and the shrunken channels being more positively charged. In comparison, the channels of the monopore AA structure are more evenly and weakly charged. This highlights the potentially profound impacts of this newly identified structure on not only the regulation of channels' dimensions but also their physical and chemical environments.

#### Universality of the Identified Dual-Pore Structure.

According to DFT calculation results, the dual-pore structure is thermodynamically favorable and therefore destined to be obtained in TAPB-DMPDA and other COFs with the same scaffold, provided there are no kinetic factors dominating the synthesis. To verify this hypothesis, we synthesized a series of TAPB-DMPDA samples and characterized them using SAXS, with the low-angle reflection at  $\sim 1.6^\circ$  serving as an indication of

the dual-pore structure. We first synthesized three samples using the aforementioned method but with varying reaction temperatures. We found that their crystallinity increases with reaction temperature, with the low-angle reflection becoming apparent above  $90^\circ\text{C}$  (Figure S9a). Moreover, we examined two samples synthesized using methods reported by Jiang's group<sup>10</sup> and Marder's group.<sup>34</sup> Despite relatively lower crystallinity, the characteristic low-angle reflection was discernible in their SAXS patterns (Figure S9b). Additionally, we synthesized two other COFs with the same framework as TAPB-DMPDA, but with hydroxyl<sup>45</sup> or prop-2-yn-1-yloxy<sup>46</sup> groups substituting the methoxy groups. These COFs also exhibited the dual-pore structure, as evidenced by SAXS and HRTEM analyses (Figures S10–S13). These results substantiate that the dual-pore structure is universal for TAPB-DMPDA-related COFs and can be easily recognized when the material's crystallinity is sufficiently high. However, it is worth noting that the monopore structure cannot be ruled out for all 2D imine-linked COFs with the same topology, given the complex factors influencing structural formation. Our ongoing research indicates that a monopore structure can form in a related system by altering the substitution groups. These findings will be reported separately in the future.

**Diverse Grain Boundary Structures.** In addition to the previously unknown bulk structure, TAPB-DMPDA exhibits abundant local structures, which are easily recognizable from the distinct contrast in the low-magnification (S)TEM images (Figure S14). We performed ULD-HRTEM to investigate these local structures in detail. Figure 5a displays a typical interfacial structure observed in TAPB-DMPDA, where two grains with the same orientation are interconnected through two rows of round 6-MR pores, forming a twin boundary. To accommodate the connection of two round 6-MR pores, the shared edge needs to be straight, adopting the *trans* conformation. Consequently, the interface region possesses two types of nonstandard 6-MR pores: five *cis* edges combined with one *trans* edge and four *cis* edges combined with two *trans* edges. As these interfacial structures do not significantly deviate from the bulk structure,

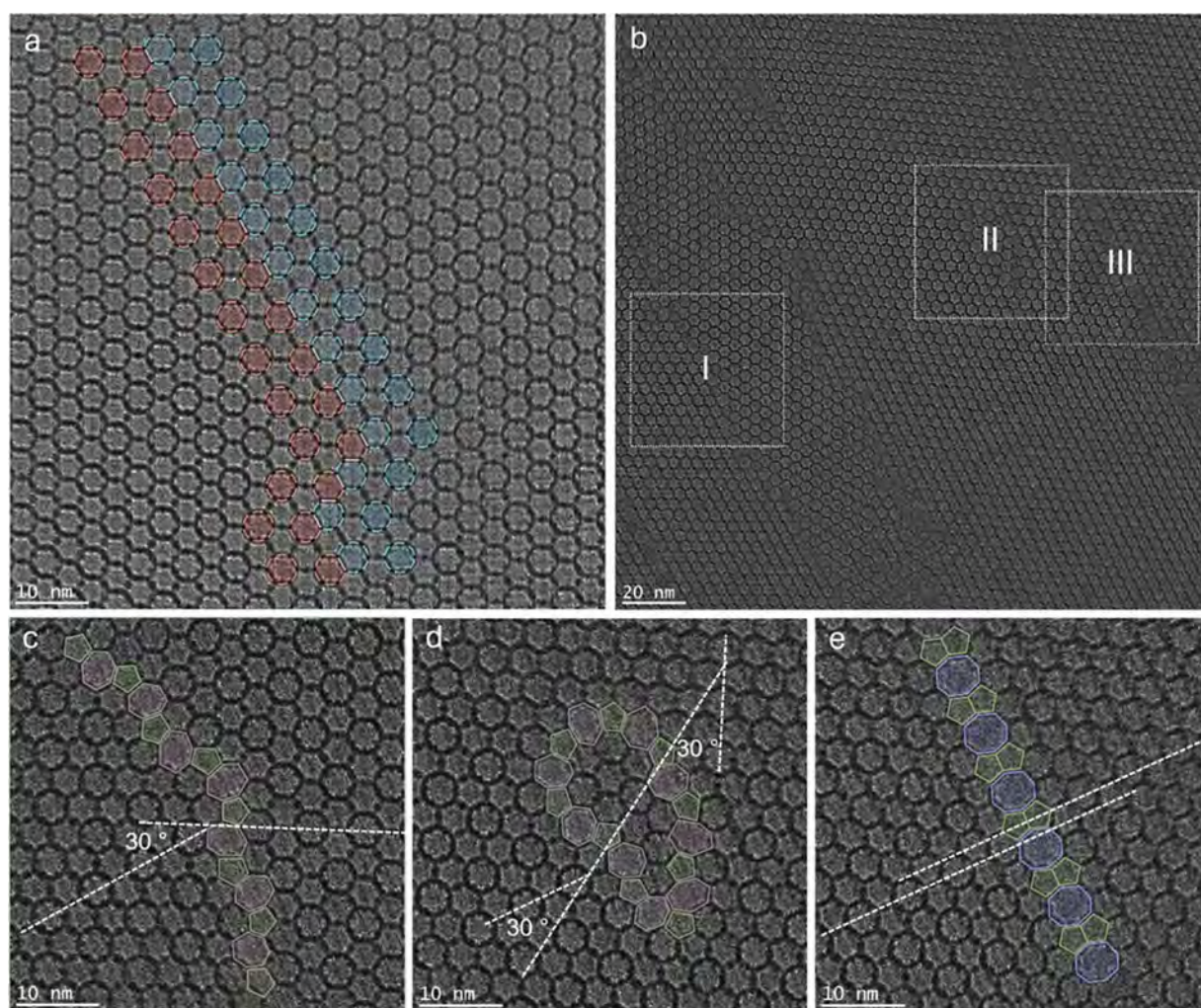


**Figure 5.** Diverse grain boundary structures in TAPB-DMPDA revealed by HRTEM. (a) Twin boundary formed between two grains with identical orientation. Nonstandard 6-MR pores are formed at the interface, with straight edges highlighted by white line segments. (b) Area exhibiting numerous defects and grain boundaries, as evidenced by the diffraction contrast in the image. (c) Enlarged view of region I in (b) showing alternating 5-MR and 7-MR pores along the boundary between two grains exhibiting a  $30^\circ$  orientation relationship. (d) Enlarged view of region II in (b) where alternating 5-MR and 7-MR pores form a loop, enclosing a small domain that is  $30^\circ$  misaligned with the surrounding area. (e) Enlarged view of region III in (b) showing a straight boundary consisting of alternating double 5-MRs and 8-MR between two grains with the same orientation but slight offset.

they are expected to have negligible effects on the material's properties.

Grain boundaries (GBs) containing non-6-MR pores are also frequently observed, as exemplified by the three areas marked in Figure 5b, with enlarged images shown in Figure 5c–e. When two grains with a  $30^\circ$  orientation relationship meet, the resulting GB is typically not straight, comprising alternating 5-MR and 7-MR pores (Figure 5c).<sup>35</sup> Occasionally, this type of GB, featuring alternating 5-MR and 7-MR pores, can form a loop, enclosing a small domain as an island that is  $30^\circ$  misaligned with the surrounding area (Figure 5d). Another prevalent GB structure identified in TAPB-DMPDA involves grains sharing identical orientations but offset by half the diameter of a 6-MR pore. In this situation, the GB is straight, consisting of alternating double 5-MRs and 8-MR pores (Figure 5e). The observed diverse non-6-MR pores are reminiscent of graphene, which has similar GB structures, albeit at the atomic scale.<sup>47</sup> The larger pore diameters of 7-MRs and 8-MRs, compared to the standard 6-MRs, would significantly influence TAPB-DMPDA's size- and shape-selectivity when employed as a separation medium or in catalysis. Being aware of their presence and knowing their

density is crucial for understanding their performance in various applications.

## CONCLUSION

Real-space imaging has revealed a previously unknown dual-pore AA'-stacking structure in the extensively studied COF, TAPB-DMPDA. This discovery is corroborated by reciprocal-space characterizations, including SAXS, SAED, and 3DED, and further substantiated by solid-state NMR and DFT calculations. Compared to the previously perceived structure, the newly identified structure exhibits variations in both pore size distribution and charge distribution, suggesting significantly different physicochemical properties. Furthermore, the identified structure has been consistently observed for this COF and structurally related COFs sharing the same framework, regardless of synthetic conditions. Additionally, real-space imaging directly uncovers the presence of numerous defects and diverse grain boundaries, including previously unknown nonstandard 6-MR, alternating 5-MR and 7-MR, as well as alternating double 5-MRs and 8-MR pore structures. The findings of this study, suggesting that both *cis* and *trans*

conformations of diimine bonds can coexist in an ordered manner, are believed to represent a general phenomenon across various imine-based COFs. Our research provides important insights into the applications of imine-based COFs, one of the most significant COF families, in separation and catalysis. It is worth noting that several effective methods for synthesizing large single crystals of COFs have been reported recently,<sup>22,25,27</sup> enabling the resolution of COF structures using single-crystal X-ray diffraction. While these methods are not yet applicable to TAPB-DMPDA, we anticipate that TAPB-DMPDA could eventually be grown into large single crystals. When this becomes possible, the dual-pore AA' structure identified in this study can be further validated through single-crystal X-ray diffraction.

## ■ ASSOCIATED CONTENT

### Data Availability Statement

All data are available in the main text or the [Supporting Information](#).

### SI Supporting Information

The Supporting Information is available free of charge at <https://pubs.acs.org/doi/10.1021/jacs.4c16678>.

Section of Materials and Methods, and additional characterization of COFs including TEM images, AFM images, iDPC-STEM images, N<sub>2</sub> adsorption, and SAXS patterns ([PDF](#))

## ■ AUTHOR INFORMATION

### Corresponding Authors

**Daliang Zhang** – Multi-scale Porous Materials Center, Institute of Advanced Interdisciplinary Studies & School of Chemistry and Chemical Engineering, Chongqing University, Chongqing 400044, China; Email: [daliang.zhang@cqu.edu.cn](mailto:daliang.zhang@cqu.edu.cn)

**Yu Wang** – School of Emergent Soft Matter, South China University of Technology, Guangzhou 510640, China; Center for Electron Microscopy and Guangdong Provincial Key Laboratory of Functional and Intelligent Hybrid Materials and Devices, South China Advanced Institute for Soft Matter Science and Technology, South China University of Technology, Guangzhou 510640, China; Email: [roywangyu@scut.edu.cn](mailto:roywangyu@scut.edu.cn)

**Zhehao Huang** – School of Emergent Soft Matter, South China University of Technology, Guangzhou 510640, China; Center for Electron Microscopy, South China University of Technology, Guangzhou 510640, China; Guangdong Basic Research Center of Excellence for Energy & Information Polymer Materials, Guangzhou 510640, China; [orcid.org/0000-0002-4575-7870](https://orcid.org/0000-0002-4575-7870); Email: [zhehaohuang@scut.edu.cn](mailto:zhehaohuang@scut.edu.cn)

**Zhiping Lai** – Physical Science and Engineering Division (PSE), Advanced Membranes and Porous Materials (AMPM) Center, King Abdullah University of Science and Technology (KAUST), Thuwal 23955-6900, Saudi Arabia; [orcid.org/0000-0001-9555-6009](https://orcid.org/0000-0001-9555-6009); Email: [zhiping.lai@kaust.edu.sa](mailto:zhiping.lai@kaust.edu.sa)

**Yu Han** – School of Emergent Soft Matter, South China University of Technology, Guangzhou 510640, China; Center for Electron Microscopy and State Key Laboratory of Pulp and Paper Engineering, South China University of Technology, Guangzhou 510640, China; Guangdong Basic Research Center of Excellence for Energy & Information Polymer Materials, Guangzhou 510640, China; [orcid.org/0000-0003-1462-1118](https://orcid.org/0000-0003-1462-1118); Email: [hanyu@scut.edu.cn](mailto:hanyu@scut.edu.cn)

## Authors

**Cailing Chen** – Physical Science and Engineering Division (PSE), Advanced Membranes and Porous Materials (AMPM) Center, King Abdullah University of Science and Technology (KAUST), Thuwal 23955-6900, Saudi Arabia; [orcid.org/0000-0003-2598-1354](https://orcid.org/0000-0003-2598-1354)

**Li Cao** – Physical Science and Engineering Division (PSE), Advanced Membranes and Porous Materials (AMPM) Center, King Abdullah University of Science and Technology (KAUST), Thuwal 23955-6900, Saudi Arabia; [orcid.org/0000-0002-7087-9431](https://orcid.org/0000-0002-7087-9431)

**Yaozu Liu** – State Key Laboratory of Inorganic Synthesis and Preparative Chemistry, College of Chemistry, Jilin University, Changchun 130012, China

**Zhihao Li** – School of Emergent Soft Matter, South China University of Technology, Guangzhou 510640, China; Center for Electron Microscopy and Guangdong Provincial Key Laboratory of Functional and Intelligent Hybrid Materials and Devices, South China Advanced Institute for Soft Matter Science and Technology, South China University of Technology, Guangzhou 510640, China

**Zhen-Hua Li** – State Key Laboratory of Inorganic Synthesis and Preparative Chemistry, College of Chemistry, Jilin University, Changchun 130012, China; [orcid.org/0000-0002-4939-2549](https://orcid.org/0000-0002-4939-2549)

**Guojun Zhou** – Department of Materials and Environmental Chemistry, Stockholm University, Stockholm SE-10691, Sweden

**Xuehai Huang** – School of Emergent Soft Matter, South China University of Technology, Guangzhou 510640, China; Center for Electron Microscopy and Guangdong Provincial Key Laboratory of Functional and Intelligent Hybrid Materials and Devices, South China Advanced Institute for Soft Matter Science and Technology, South China University of Technology, Guangzhou 510640, China

**Guanxing Li** – Physical Science and Engineering Division (PSE), Advanced Membranes and Porous Materials (AMPM) Center, King Abdullah University of Science and Technology (KAUST), Thuwal 23955-6900, Saudi Arabia

**Lingmei Liu** – Multi-scale Porous Materials Center, Institute of Advanced Interdisciplinary Studies & School of Chemistry and Chemical Engineering, Chongqing University, Chongqing 400044, China; [orcid.org/0000-0002-3273-9884](https://orcid.org/0000-0002-3273-9884)

**You-You Yuan** – Imaging and Characterization Core Lab, King Abdullah University of Science and Technology (KAUST), Thuwal 23955-6900, Saudi Arabia

**Yaping Zhang** – Imaging and Characterization Core Lab, King Abdullah University of Science and Technology (KAUST), Thuwal 23955-6900, Saudi Arabia

**Qingxiao Wang** – Imaging and Characterization Core Lab, King Abdullah University of Science and Technology (KAUST), Thuwal 23955-6900, Saudi Arabia

**Yiqiang Chen** – Imaging and Characterization Core Lab, King Abdullah University of Science and Technology (KAUST), Thuwal 23955-6900, Saudi Arabia

**Zhan Shi** – State Key Laboratory of Inorganic Synthesis and Preparative Chemistry, College of Chemistry, Jilin University, Changchun 130012, China; [orcid.org/0000-0001-9717-1487](https://orcid.org/0000-0001-9717-1487)

**Qianrong Fang** – State Key Laboratory of Inorganic Synthesis and Preparative Chemistry, College of Chemistry, Jilin University, Changchun 130012, China; [orcid.org/0000-0003-3365-5508](https://orcid.org/0000-0003-3365-5508)

Complete contact information is available at:  
<https://pubs.acs.org/10.1021/jacs.4c16678>

### Author Contributions

<sup>††</sup>C.C., L.C., Y.L., Z.L. and Z.-H.L. contributed equally to this work.

### Notes

The authors declare no competing financial interest.

## ACKNOWLEDGMENTS

This research was supported by National Key Research and Development Project of China (2022YFE0113800) and KAUST Baseline Fund (BAS/1/1375-01-01). Y.H. thanks the research fund from State Key Laboratory of Pulp and Paper Engineering, South China University of Technology (2024ZD03). Z.H. acknowledges the Guangdong Basic and Applied Basic Research Foundation (2024B1515020078), the Swedish Research Council Formas (2020-00831), and the Swedish Research Council (VR, 2022-02939) for funding support.

## REFERENCES

- (1) Novoselov, K. S.; Geim, A. K.; Morozov, S. V.; Jiang, D.; Zhang, Y.; Dubonos, S. V.; Grigorieva, I. V.; Firsov, A. A. Electric field effect in atomically thin carbon films. *Science* **2004**, *306* (5696), 666–669.
- (2) Head-Gordon, T.; Hura, G. Water structure from scattering experiments and simulation. *Chem. Rev.* **2002**, *102* (8), 2651–2670.
- (3) Hura, G.; Russo, D.; Glaeser, R. M.; Head-Gordon, T.; Krack, M.; Parrinello, M. Water structure as a function of temperature from X-ray scattering experiments and ab initio molecular dynamics. *Phys. Chem. Chem. Phys.* **2003**, *5* (10), 1981–1991.
- (4) Smith, J. D.; Cappa, C. D.; Wilson, K. R.; Messer, B. M.; Cohen, R. C.; Saykally, R. J. Energetics of hydrogen bond network rearrangements in liquid water. *Science* **2004**, *306* (5697), 851–853.
- (5) Wernet, P.; Nordlund, D.; Bergmann, U.; Cavalleri, M.; Odelius, M.; Ogasawara, H.; Näslund, L. A.; Hirsch, T. K.; Ojamäe, L.; Glatzel, P.; Pettersson, L. G.; Nilsson, A. The structure of the first coordination shell in liquid water. *Science* **2004**, *304* (5673), 995–999.
- (6) Cote, A. P.; Benin, A. I.; Ockwig, N. W.; O’Keeffe, M.; Matzger, A. J.; Yaghi, O. M. Porous, crystalline, covalent organic frameworks. *Science* **2005**, *310* (5751), 1166–1170.
- (7) Feng, X.; Ding, X.; Jiang, D. Covalent organic frameworks. *Chem. Soc. Rev.* **2012**, *41* (18), 6010–6022.
- (8) Lee, J. M.; Cooper, A. I. Advances in conjugated microporous polymers. *Chem. Rev.* **2020**, *120* (4), 2171–2214.
- (9) Geng, K.; He, T.; Liu, R.; Dalapati, S.; Tan, K. T.; Li, Z.; Tao, S.; Gong, Y.; Jiang, Q.; Jiang, D. Covalent organic frameworks: Design, synthesis, and functions. *Chem. Rev.* **2020**, *120* (16), 8814–8933.
- (10) Xu, H.; Gao, J.; Jiang, A. Stable, crystalline, porous, covalent organic frameworks as a platform for chiral organocatalysts. *Nat. Chem.* **2015**, *7* (11), 905–912.
- (11) Yuan, Y.; Yang, Y.; Meihaus, K. R.; Zhang, S.; Ge, X.; Zhang, W.; Faller, R.; Long, J. R.; Zhu, G. Selective scandium ion capture through coordination templating in a covalent organic framework. *Nat. Chem.* **2023**, *15* (11), 1599–1606.
- (12) Wang, Z.; Zhang, S.; Chen, Y.; Zhang, Z.; Ma, S. Covalent organic frameworks for separation applications. *Chem. Soc. Rev.* **2020**, *49* (3), 708–735.
- (13) Liu, X.; Huang, D.; Lai, C.; Zeng, G.; Qin, L.; Wang, H.; Yi, H.; Li, B.; Liu, S.; Zhang, M.; Deng, R.; Fu, Y.; Li, L.; Xue, W.; Chen, S. Recent advances in covalent organic frameworks (COFs) as a smart sensing material. *Chem. Soc. Rev.* **2019**, *48* (20), 5266–5302.
- (14) Kang, C.; Zhang, Z.; Wee, V.; Usadi, A. K.; Calabro, D. C.; Baugh, L. S.; Wang, S.; Wang, Y.; Zhao, D. Interlayer shifting in two-dimensional covalent organic frameworks. *J. Am. Chem. Soc.* **2020**, *142* (30), 12995–13002.
- (15) Li, Y.; Guo, L.; Lv, Y.; Zhao, Z.; Ma, Y.; Chen, W.; Xing, G.; Jiang, D.; Chen, L. Polymorphism of 2D imine covalent organic frameworks. *Angew. Chem., Int. Ed.* **2021**, *60* (10), 5363–5369.
- (16) Zhang, W.; Chen, L.; Dai, S.; Zhao, C.; Ma, C.; Wei, L.; Zhu, M.; Chong, S. Y.; Yang, H.; Liu, L.; Bai, Y.; Yu, M.; Xu, Y.; Zhu, X. W.; Zhu, Q.; An, S.; Sprick, R. S.; Little, M. A.; Wu, X.; Jiang, S.; Wu, Y.; Zhang, Y. B.; Tian, H.; Zhu, W. H.; Cooper, A. I. Reconstructed covalent organic frameworks. *Nature* **2022**, *604* (7904), 72–79.
- (17) Pelkowski, C. E.; Natraj, A.; Malliakas, C. D.; Burke, D. W.; Bardot, M. I.; Wang, Z.; Li, H.; Dichtel, W. R. Tuning crystallinity and stacking of two-dimensional covalent organic frameworks through side-chain interactions. *J. Am. Chem. Soc.* **2023**, *145* (40), 21798–21806.
- (18) Haase, F.; Troschke, E.; Savasci, G.; Banerjee, T.; Duppel, V.; Dorfler, S.; Grundei, M. M. J.; Burow, A. M.; Ochsenfeld, C.; Kaskel, S.; Lotsch, B. V. Topochemical conversion of an imine- into a thiazole-linked covalent organic framework enabling real structure analysis. *Nat. Commun.* **2018**, *9* (1), 2600.
- (19) Qi, H.; Sahabudeen, H.; Liang, B.; Polozij, M.; Addicoat, M. A.; Gorelik, T. E.; Hamsch, M.; Mundsinger, M.; Park, S.; Lotsch, B. V.; Mannsfeld, S. C. B.; Zheng, Z.; Dong, R.; Heine, T.; Feng, X.; Kaiser, U. Near-atomic-scale observation of grain boundaries in a layer-stacked two-dimensional polymer. *Sci. Adv.* **2020**, *6* (33), No. eabb5976.
- (20) Zhan, G.; Cai, Z. F.; Strutyński, K.; Yu, L.; Herrmann, N.; Martínez-Abadía, M.; Melle-Franco, M.; Mateo-Alonso, A.; Feyter, S. Observing polymerization in 2D dynamic covalent polymers. *Nature* **2022**, *603* (7903), 835–840.
- (21) Yang, Y.; Liang, B.; Kreie, J.; Hamsch, M.; Liang, Z.; Wang, C.; Huang, S.; Dong, X.; Gong, L.; Liang, C.; Lou, D.; Zhou, Z.; Lu, J.; Yang, Y.; Zhuang, X.; Qi, H.; Kaiser, U.; Mannsfeld, S. C. B.; Liu, W.; Golzhauser, A.; Zheng, Z. Elastic films of single-crystal two-dimensional covalent organic frameworks. *Nature* **2024**, *630*, 878–883.
- (22) Ma, T.; Kapustin, E. A.; Yin, S. X.; Liang, L.; Zhou, Z.; Niu, J.; Li, L. H.; Wang, Y.; Su, J.; Li, J.; Wang, X.; Wang, W. D.; Wang, W.; Sun, J.; Yaghi, O. M. Single-crystal x-ray diffraction structures of covalent organic frameworks. *Science* **2018**, *361* (6397), 48–52.
- (23) Qian, C.; Feng, L.; Teo, W. L.; Liu, J.; Zhou, W.; Wang, D.; Zhao, Y. Imine and imine-derived linkages in two-dimensional covalent organic frameworks. *Nat. Rev. Chem.* **2022**, *6* (12), 881–898.
- (24) Kang, C.; Zhang, Z.; Kusaka, S.; Negita, K.; Usadi, A. K.; Calabro, D. C.; Baugh, L. S.; Wang, Y.; Zou, X.; Huang, Z.; Matsuda, R.; Zhao, D. Covalent organic framework atropisomers with multiple gas-triggered structural flexibilities. *Nat. Mater.* **2023**, *22*, 636–643.
- (25) Han, J.; Feng, J.; Kang, J.; Chen, J. M.; Du, X. Y.; Ding, S. Y.; Liang, L.; Wang, W. Fast growth of single-crystal covalent organic frameworks for laboratory x-ray diffraction. *Science* **2024**, *383* (6686), 1014–1019.
- (26) Gruber, C. G.; Frey, L.; Guntermann, R.; Medina, D. D.; Cortes, E. Early stages of covalent organic framework formation imaged in operando. *Nature* **2024**, *630*, 872–877.
- (27) Yi, L.; Gao, Y.; Luo, S.; Wang, T.; Deng, H. Structure evolution of 2D covalent organic frameworks unveiled by single-crystal X-ray diffraction. *J. Am. Chem. Soc.* **2024**, *146*, 19643–19648.
- (28) Xu, H.; Tao, S.; Jiang, D. Proton conduction in crystalline and porous covalent organic frameworks. *Nat. Mater.* **2016**, *15* (7), 722–726.
- (29) Natraj, A.; Ji, W.; Xin, J.; Castano, I.; Burke, D. W.; Evans, A. M.; Strauss, M. J.; Ateia, M.; Hamachi, L. S.; Gianneschi, N. C.; Alothman, Z. A.; Sun, J.; Yusuf, K.; Dichtel, W. R. Single-crystalline imine-linked two-dimensional covalent organic frameworks separate benzene and cyclohexane efficiently. *J. Am. Chem. Soc.* **2022**, *144* (43), 19813–19824.
- (30) Kang, C.; Zhang, Z.; Usadi, A. K.; Calabro, D. C.; Baugh, L. S.; Chai, K.; Wang, Y.; Zhao, D. Tunable interlayer shifting in two-dimensional covalent organic frameworks triggered by CO<sub>2</sub> sorption. *J. Am. Chem. Soc.* **2022**, *144* (44), 20363–20371.
- (31) Kang, C.; Zhang, Z.; Usadi, A. K.; Calabro, D. C.; Baugh, L. S.; Yu, K.; Wang, Y.; Zhao, D. Aggregated structures of two-dimensional covalent organic frameworks. *J. Am. Chem. Soc.* **2022**, *144* (7), 3192–3199.

- (32) Natraj, A.; Landman, I. R.; Pelkowski, C. E.; Burke, D. W.; Kewalramani, S.; Dichtel, W. R. Nonclassical crystallization processes of single-crystalline two-dimensional covalent organic frameworks. *J. Am. Chem. Soc.* **2024**, *146*, 16775–16786.
- (33) Li, X.; Zhang, C.; Cai, S.; Lei, X.; Altoe, V.; Hong, F.; Urban, J. J.; Ciston, J.; Chan, E. M.; Liu, Y. Facile transformation of imine covalent organic frameworks into ultrastable crystalline porous aromatic frameworks. *Nat. Commun.* **2018**, *9* (1), 2998.
- (34) Feriante, C. H.; Jhulki, S.; Evans, A. M.; Dasari, R. R.; Slicker, K.; Dichtel, W. R.; Marder, S. R. Rapid synthesis of high surface area imine-linked 2D covalent organic frameworks by avoiding pore collapse during isolation. *Adv. Mater.* **2020**, *32* (2), No. e1905776.
- (35) Zhu, Y. H.; Ciston, J.; Zheng, B.; Miao, X. H.; Czarnik, C.; Pan, Y. C.; Sougrat, R.; Lai, Z. P.; Hsiung, C. E.; Yao, K. X.; Pinnau, I.; Pan, M.; Han, Y. Unravelling surface and interfacial structures of a metal-organic framework by transmission electron microscopy. *Nat. Mater.* **2017**, *16* (5), 532–536.
- (36) Zhang, D. L.; Zhu, Y. H.; Liu, L. M.; Ying, X. R.; Hsiung, C. E.; Sougrat, R.; Li, K.; Han, Y. Atomic-resolution transmission electron microscopy of electron beam-sensitive crystalline materials. *Science* **2018**, *359* (6376), 675–679.
- (37) Li, X.; Wang, J.; Liu, X.; Liu, L.; Cha, D.; Zheng, X.; Yousef, A. A.; Song, K.; Zhu, Y.; Zhang, D.; Han, Y. Direct imaging of tunable crystal surface structures of MOF MIL-101 using high-resolution electron microscopy. *J. Am. Chem. Soc.* **2019**, *141* (30), 12021–12028.
- (38) Liu, L.; Chen, Z.; Wang, J.; Zhang, D.; Zhu, Y.; Ling, S.; Huang, K. W.; Belmabkhout, Y.; Adil, K.; Zhang, Y.; Slater, B.; Eddaoudi, M.; Han, Y. Imaging defects and their evolution in a metal-organic framework at sub-unit-cell resolution. *Nat. Chem.* **2019**, *11* (7), 622–628.
- (39) Chen, C.; Meng, L.; Cao, L.; Zhang, D.; An, S.; Liu, L.; Wang, J.; Li, G.; Pan, T.; Shen, J.; Chen, Z.; Shi, Z.; Lai, Z.; Han, Y. Phase engineering of zirconium MOFs enables efficient osmotic energy conversion: structural evolution unveiled by direct imaging. *J. Am. Chem. Soc.* **2024**, *146* (17), 11855–11865.
- (40) Halder, A.; Kandambeth, S.; Biswal, B. P.; Kaur, G.; Roy, N. C.; Addicoat, M.; Salunke, J. K.; Banerjee, S.; Vanka, K.; Heine, T.; Verma, S.; Banerjee, R. Decoding the morphological diversity in two dimensional crystalline porous polymers by core planarity modulation. *Angew. Chem., Int. Ed.* **2016**, *55* (27), 7806–7810.
- (41) Peng, Y.; Li, L.; Zhu, C.; Chen, B.; Zhao, M.; Zhang, Z.; Lai, Z.; Zhang, X.; Tan, C.; Han, Y.; Zhu, Y.; Zhang, H. Intramolecular hydrogen bonding-based topology regulation of two-dimensional covalent organic frameworks. *J. Am. Chem. Soc.* **2020**, *142* (30), 13162–13169.
- (42) Ou, Z.; Liang, B.; Liang, Z.; Tan, F.; Dong, X.; Gong, L.; Zhao, P.; Wang, H.; Zou, Y.; Xia, Y.; Chen, X.; Liu, W.; Qi, H.; Kaiser, U.; Zheng, Z. Oriented growth of thin films of covalent organic frameworks with large single-crystalline domains on the water surface. *J. Am. Chem. Soc.* **2022**, *144* (7), 3233–3241.
- (43) Johnson, E. R.; Keinan, S.; Mori-Sanchez, P.; Contreras-Garcia, J.; Cohen, A. J.; Yang, W. Revealing noncovalent interactions. *J. Am. Chem. Soc.* **2010**, *132* (18), 6498–6506.
- (44) Lu, T.; Manzetti, S. Wavefunction and reactivity study of benzo[a]pyrene diol epoxide and its enantiomeric forms. *Struct. Chem.* **2014**, *25* (5), 1521–1533.
- (45) Kandambeth, S.; Venkatesh, V.; Shinde, D. B.; Kumari, S.; Halder, A.; Verma, S.; Banerjee, R. Self-templated chemically stable hollow spherical covalent organic framework. *Nat. Commun.* **2015**, *6*, 6786.
- (46) Jing, X.; Zhang, M.; Mu, Z.; Shao, P.; Zhu, Y.; Li, J.; Wang, B.; Feng, X. Gradient channel segmentation in covalent organic framework membranes with highly oriented nanochannels. *J. Am. Chem. Soc.* **2023**, *145* (38), 21077–21085.
- (47) Huang, P. Y.; Ruiz-Vargas, C. S.; van der Zande, A. M.; Whitney, W. S.; Levendoff, M. P.; Kevek, J. W.; Garg, S.; Alden, J. S.; Hustedt, C. J.; Zhu, Y.; Park, J.; McEuen, P. L.; Muller, D. A. Grains and grain boundaries in single-layer graphene atomic patchwork quilts. *Nature* **2011**, *469* (7330), 389–392.